WARWICK
THE UNIVERSITY OF WARWICK

Manuscript version: Author's Accepted Manuscript
The version presented in WRAP is the author's accepted manuscript and may differ from the published version or Version of Record.

Persistent WRAP URL:
http://wrap.warwick.ac.uk/134487

How to cite:
Please refer to published version for the most recent bibliographic citation information. If a published version is known of, the repository item page linked to above, will contain details on accessing it.

Copyright and reuse:
The Warwick Research Archive Portal (WRAP) makes this work by researchers of the University of Warwick available open access under the following conditions.

© 2020 Elsevier. Licensed under the Creative Commons Attribution-NonCommercial-NoDerivatives 4.0 International http://creativecommons.org/licenses/by-nc-nd/4.0/.

Publisher's statement:
Please refer to the repository item page, publisher's statement section, for further information.

For more information, please contact the WRAP Team at: wrap@warwick.ac.uk.

warwick.ac.uk/lib-publications

Surface Microstructural Controls on Electrochemical Hydrogen Absorption at Polycrystalline Palladium

Lewis C. Yule,[†,‡] Enrico Daviddi,[†] Geoff West,[‡] Cameron L. Bentley[†,*] and Patrick R. Unwin[†,*]

[†]Department of Chemistry, University of Warwick, Coventry CV4 7AL, U.K.

[‡]Warwick Manufacturing Group, University of Warwick, Coventry CV4 7AL, U.K.

Abstract. The ease by which hydrogen is absorbed into a metal can be either advantageous or deleterious, depending on the material and application in question. For instance, in metals such as palladium (Pd), rapid absorption kinetics are seen as a beneficial property for hydrogen purification and storage applications, whereas the contrary is true for structural metals such as steel, which are susceptible to mechanical degradation in a process known as hydrogen embrittlement. It follows that understanding how the microstructure of metals (*i.e.*, grains and grain boundaries) influences adsorption and absorption kinetics would be extremely powerful to rationally design materials (*e.g.*, alloys) with either a high affinity for hydrogen or resistance to hydrogen embrittlement. To this end, scanning electrochemical cell microscopy (SECCM) is deployed herein to study surface structure-dependent electrochemical hydrogen absorption across the surface of flame annealed polycrystalline Pd in aqueous sulfuric acid (considered the model system for the study of hydrogen absorption). Correlating spatially-resolved cyclic voltammetric data from SECCM with co-located structural information from electron backscatter diffraction (EBSD) reveals a clear relationship between the crystal orientation and the rate of hydrogen adsorption-absorption. Grains that are closest to the low-index orientations [*i.e.*, the {100}, {101}, and {111} facets, face-centered cubic (fcc) system] facilitate the lowest rates of hydrogen absorption, whereas grains of high-index orientation (*e.g.*, {411}) promoted higher rates. Apparently enhanced kinetics are also seen at grain boundaries, which is thought to arise from physical deformation of the Pd surface adjacent to the boundary, resulting from the flame annealing and quenching process. As voltammetric measurements are made across a wide potential range, these studies also reveal palladium oxide formation and stripping to be surface structure-dependent processes, and further highlight the power of combined SECCM-EBSD for structure-activity measurements in electrochemical science.

Hydrogen absorption into metals is of wide interest, whether for hydrogen storage in metals such as palladium (Pd), or where it adversely affects the mechanical properties of structural materials such as steel [1]. During the absorption process, surface-adsorbed hydrogen atoms, originating from dissociative chemisorption of H_2 gas or electro-reduction of H^+ from solution (*i.e.*, the cathodic process during corrosion), diffuse into the bulk metal, occupying interstitial sites within the crystal lattice [2]. This can reduce the ductility of a metal, making it brittle and at risk from cracking when subjected to stress, in a process known as hydrogen embrittlement [3, 4]. Due to the societal and industrial implications of hydrogen embrittlement, the absorption of hydrogen into steels has attracted significant research attention [5-7]. One particular area of interest has involved modifying the microstructure of steels to reduce the affinity to hydrogen, which has involved the engineering of grain boundaries and/or manipulation of texture (*i.e.*, grain structure). For instance, steels with higher grain boundary densities have been shown to promote the diffusion of hydrogen [8], whilst varying levels of hydrogen permeation have been measured between different crystal phases [9].

Palladium (Pd) is considered to be a model metal to study hydrogen absorption, due to high intrinsic hydrogen solubility and rapid entry kinetics [10, 11]. It also possesses desirable properties for hydrogen storage, as Pd forms hydrides, a relatively safe form of stored hydrogen, under ambient conditions [12]. As such, there has been considerable effort to understand and engineer the composition and structure of Pd (nano)materials for fast hydrogen uptake and release [13]. For instance, numerous studies have focused on the shape (facet) dependent hydrogen-storage properties of Pd nanoparticles (PdNPs) [14-16]. Despite being the subject of many investigations, electrochemical hydrogen absorption into Pd has largely been studied at the macroscopic level with electrochemical techniques, predominantly on polycrystalline electrodes (*e.g.*, thin films and bulk metal) [10, 11, 17], making it

difficult to unambiguously resolve the (micro)structural controls on surface activity [18]. Furthermore, the limited number of studies on structurally well-defined electrodes such as single-crystals [19] have focused exclusively on the low-index facets [*i.e.*, the {100}, {101}, and {111} facets of the face-centered cubic (fcc) system], and thus do not consider the important roles of high-energy surfaces, such as the high-index facets and grain boundaries [20, 21].

Scanning electrochemical cell microscopy (SECCM) [22, 23], a recent addition to the electrochemical droplet cell (EDC) family, is proving to be a very powerful technique for probing the spatially-dependent electrochemistry of complex electrode surfaces [18, 24]. In SECCM, electrochemical measurements are performed in a statistically large number (typically hundreds to thousands) of small areas of a surface, defined by a droplet (meniscus) cell created between a nanopipet probe filled with electrolyte solution and substrate (working electrode) surface. When applied to polycrystalline electrodes, SECCM electrochemically interrogates the individual grains and grain boundaries that constitute the surface, which is correlated to co-located structural information from electron backscatter diffraction (EBSD) to resolve nanoscale structure–activity *directly* and *unambiguously*. Indeed, this *pseudo single-crystal approach* [25] has previously been employed to investigate the grain (and grain boundary) dependent electrochemistry of polycrystalline platinum [25-28], gold [29], boron-doped diamond [30] and low carbon steel [31-33]. Building on this body of work, herein we employ SECCM in tandem with co-located EBSD to investigate grain-dependent electrochemical proton reduction coupled to hydrogen adsorption-absorption into polycrystalline Pd in aqueous sulfuric acid. Apparently enhanced electrochemical kinetics are identified at grains of high-index orientation (*e.g.*, {411}) and grain boundaries relative to the grains of low-index orientation (*i.e.*,

{100}, {101} and {111}), indicating these high-energy surfaces as important sites of electrochemical hydrogen absorption at polycrystalline Pd.

Experimental Methods

Electrode materials and chemicals. Pd foil of 0.6 mm thickness and with dimensions of 10×10 mm (Goodfellow, U.K., 99.95%), was polished on a polishing cloth (TexMat C, Buehler, U.S.A) with a polishing machine (AutoMet 3000 Pro. Buehler, U.S.A.) using 9 µm, 3 µm, and 1 µm polishing suspensions (MetaDi Supreme Diamond, Buehler, U.S.A.), respectively. The final polish was performed on a different cloth (ChemoMet, Buehler, U.S.A.) with a 0.05 µm polishing suspension (MaterPrep Alumina, Buehler, U.S.A). The polished Pd foil was washed with soapy water and subsequently deionized water to remove contamination from the polishing suspensions, before being blown dry. Immediately prior to use as a working electrode, the Pd foil was flame annealed in a butane torch flame and quenched in deionized water (resistivity = 18.2 MΩ.cm at 25°C, Integra HP, Purite, U.K.). This enlarged the average grain size (tens of micron scale, *vide infra*) and ensured that the Pd surface was pristine (*i.e.*, free from airborne contaminants) prior to SECCM scanning. Between experiments, the Pd foil substrate was stored in a vacuum at room temperature (22ºC).

Sulfuric acid (H_2SO_4, Merck, 96%) was used as supplied and diluted with deionized water. The Ag/AgCl quasi reference counter electrode (QRCE) was prepared by anodizing 0.25 mm diameter annealed Ag wire (Goodfellow, U.K., 99.99%) in saturated KCl (Honeywell, 99.5%) solution. The Ag/AgCl QRCE possessed a stable potential of *ca.* 0.23 V versus a commercial Ag/AgCl reference electrode (3.4 M KCl, ET072, eDAQ, Australia), in agreement with a previous report [34].

Surface characterization. Scanning electron microscopy (SEM) and EBSD was performed with a Zeiss SUPRA FE-SEM (Zeiss, Germany), equipped with a Nordlys EBSD detector (Oxford Instruments, U.K.). EBSD mapping was carried out with an acceleration voltage of 20 keV, with the sample tilted

70º to the detector. The EBSD data was processed using the HKL CHANNEL5 software (Tango, Oxford Instruments, U.K.).

In order to visualize the surface structure-dependent electrochemical (adsorption-absorption) kinetics, plots of grain- surface current (i_{surf}) versus crystallographic orientation relative to the low index orientations (*i.e.*, {100}, {101}, and {111}) were created. To achieve this, the Euler angles (φ_1, Φ, φ_2) that define the orientation of a plane (measured with EBSD), were first used to calculate the Miller indices {*hkl*} for each grain:

$$h = \sin(\Phi) \cdot \sin(\varphi_2) \quad \textbf{(1)}$$

$$k = \sin(\Phi) \cdot \cos(\varphi_2) \quad \textbf{(2)}$$

$$l = \cos(\Phi) \quad \textbf{(3)}$$

Using the calculated Miller indices, the deviation (θ) of the orientation of each plane {*hkl*} from any other plane $\{h^*k^*l^*\}$ was calculated as follows:

$$\cos(\theta) = \frac{hh^* + kk^* + ll^*}{\sqrt{h^2 + k^2 + l^2} \cdot \sqrt{h^{*2} + k^{*2} + l^{*2}}} \quad \textbf{(4)}$$

In the present context, $\{h^*k^*l^*\}$ refers to each of the low-index orientations, {100}, {101} and {111}, allowing each grain to be plotted in a three dimensional (3D) space, where each axis (*x*, *y*, *z*) corresponds to the deviation angle (θ) from each low-index plane, *i.e.*, (θ_{001}, θ_{011}, θ_{111}). When plotted in 3D space, all points (orientations) lay on a hyperbolic plane, due to the fact that the *x*, *y* and *z* coordinates are not linearly independent (*i.e.*, θ_{001}, θ_{011} and θ_{111} were calculated from the same two variables, Φ and φ_2). When projected onto a two-dimensional (2D) plane (represented by two arbitrary Cartesian coordinates, *x* and *y*), all grains lay in a section delimited by the functions representing the following three families of planes: {0 *n* 1}//ND, {*n* 1 1}//ND and {*n n* 1}//ND, with $0 \leq n \leq 1$, as shown in Scheme 1, below.

Finally, each point representing a grain was colored based on average i_{surf} measured on that grain (*i.e.*, from SECCM scanning) adopting an independent color bar scale, allowing the electrochemical hydrogen absorption activity as a function of grain structure to be readily visualized.

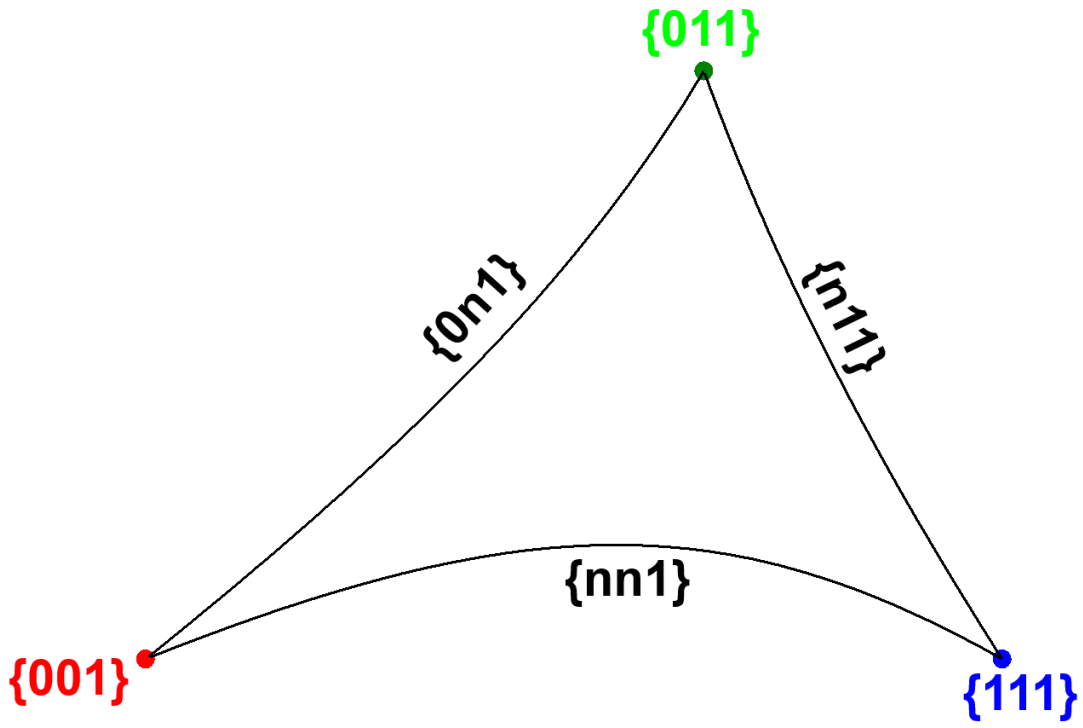

Scheme 1. Two-dimensional projection of grain orientations in a fcc cubic crystal system, represented in arbitrary coordinates. The black lines delineate the space that contains all possible grain orientations (given the symmetry of the cubic system). In the above projection, *n* is any real number between 0 and 1.

Electrochemical systems and measurements. Macroscopic cyclic voltammetry was performed in a conventional three-electrode format on an FAS2 Femtostat (Gamry, U.S.A.), with a Pd wire working electrode (length ≈ 1.7 cm, diameter ≈ 0.025 cm, Goodfellow, U.K., 99.95%), Ag/AgCl wire reference electrode and Pt wire (diameter = 0.5 mm, Goodfellow) counter electrode. All other electrochemical experiments were performed in the SECCM format on a home-built scanning electrochemical probe microscopy (SEPM) workstation [35, 36].

SECCM was operated in the voltammetric hopping mode with a single-channeled nanopipet, shown schematically in Figure 1a [37, 38]. In brief, a nanopipet, laser pulled from borosilicate capillaries (GC120F-10, Harvard Apparatus, U.S.A.), was filled with 0.5 M H_2SO_4 and fitted with an Ag/AgCl QRCE. During operation, the nanopipet probe was mounted on a *z*-piezoelectric positioner (P-753.2 LISA; PhysikInstrumente, Germany) and positioned above the Pd foil substrate. The substrate was mounted on an *xy*-piezoelectric positioner (P-621.2 PIHera, PhysikInstrumente). Each axis was also equipped with a micropositioner for coarse movement. During scanning, the nanopipet probe was approached to the surface of interest while applying a potential, $-E_{app}$, at the Ag/AgCl QRCE within the probe, such that a current, i_{surf}, would flow upon meniscus contact (*i.e.*, upon closing the electrochemical circuit). This was used as a feedback signal to halt the approach of the nanopipet. After meniscus-surface contact was established, multiple iterations of cyclic voltammetry were performed (*e.g.*, potential-time and current-time waveforms shown in Figure 1b) within the confined meniscus electrochemical cell. After the cyclic voltammetric measurement was complete, the probe was retracted and moved to a new scanning site located within a pre-programmed grid, building up a dynamic electrochemical "map" of the Pd surface. Note that oxygen (O_2) was excluded from the SECCM droplet cell through the use of an argon-purged environmental cell (argon flow rate of 60 cm^3/min), as previously reported [39].

The entire SEPM set up was situated on a vibration isolation platform (BM-8, Minus K, U.S.A.), located within an aluminum faraday cage equipped with heat sinks and acoustic foam. This configuration has previously been shown to minimize electrical noise, thermal drift and mechanical vibration [38, 40]. The QRCE potential was controlled, with respect to ground, and the current flowing at the Pd foil working electrode (*i.e.*, i_{surf}), held at a common ground, was measured using a home-built electrometer. i_{surf} was measured every 4 µs, which was averaged 256 times to give a data acquisition

rate of 4 × (256 + 1) = 1028 µs (note that one extra iteration is used to transfer the data to the host computer). Data acquisition and instrumental control was carried out using an FPGA card (PCIe-7852R) controlled by a LabVIEW 2016 (National Instruments, U.S.A.) interface, running the Warwick Electrochemical Scanning Probe Microscopy (WEC-SPM, *www.warwick.ac.uk/electrochemistry*) software.

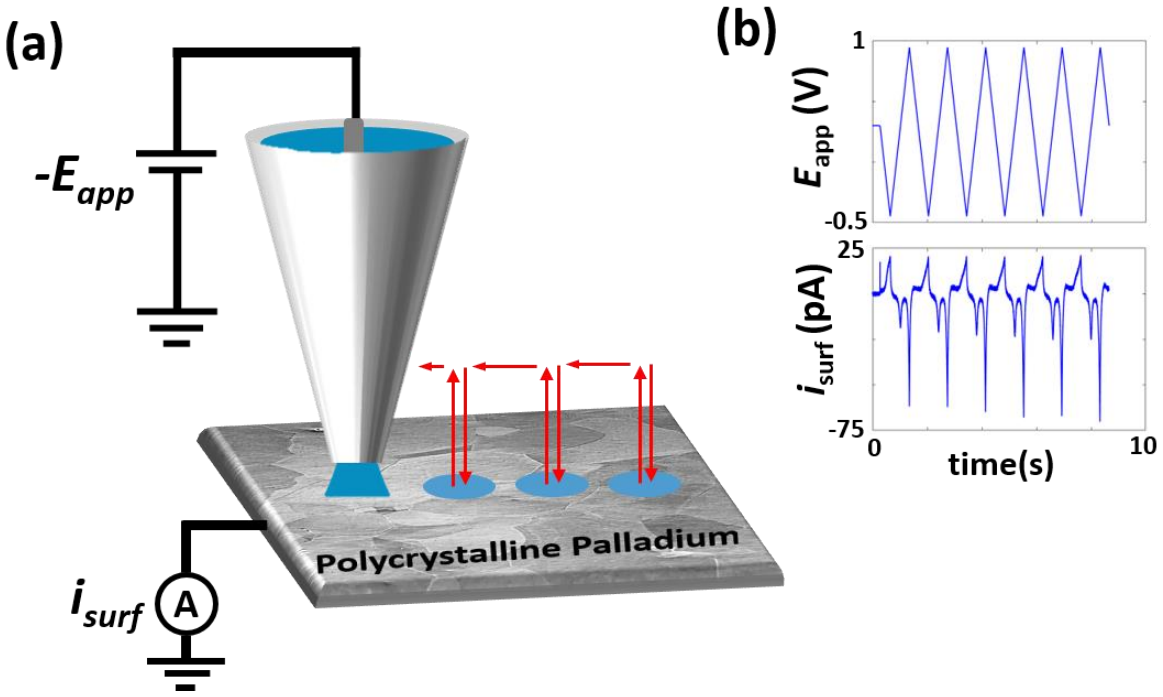

Figure 1. (a) Schematic of the voltammetric hopping-mode SECCM configuration used in this study. The red arrows indicate the path taken by the nanopipet probe during scanning. The nanopipet was filled with 0.5 M H_2SO_4 and equipped with an Ag/AgCl QRCE. **(b)** Plots of the applied potential, E_{app}, and surface current, i_{surf}, as a function of time during the meniscus-surface contact period from a single 'hop' of a scanning experiment. During scanning, a cyclic voltammetric waveform was applied, sweeping the potential between *ca.* 0.95 and −0.45 V vs. Ag/AgCl at a voltammetric scan rate (υ) of 2 V s^{-1}, for a total of 6 potential cycles at each meniscus contact.

Results and Discussion

Cyclic voltammetry on Pd: macroscale *vs* nanoscale. The macroscopic voltammetric (current-voltage, *i*−*E*) response of polycrystalline Pd was initially investigated in de-aerated 0.5 M H_2SO_4; a typical cyclic voltammogram (CV) is shown in Figure 2a. Oxidative processes attributable to palladium oxide (PdO_x) formation are observed at potentials above *ca.* 0.2 V *vs* Ag/AgCl wire on the anodic sweep, with the corresponding (symmetrical) reductive PdO_x stripping peak, also centered around 0.2 V on cathodic sweep. Both of these processes develop with potential cycling, indicating that the Pd wire undergoes dynamic surface restructuring and/or roughening within this potential range. By contrast, the rate of the hydrogen adsorption-absorption reaction, occurring at potentials negative of *ca.* − 0.15 V *vs* Ag/AgCl, does not change significantly with potential cycling. Note that due to the high intrinsic hydrogen solubility and rapid entry kinetics in Pd [10, 11], as well as the fact that the applied potentials are positive of the expected onset of the hydrogen evolution reaction (HER) on Pd (*i.e.*, 0 V *vs* the reversible hydrogen electrode, RHE, corresponding to *ca.* −0.47 V *vs* Ag/AgCl, herein) [41], the measured current must arise solely from net hydrogen adsorption-absorption. The voltammetric behavior of Pd in Figure 1a is consistent with previous studies on the bulk material [11, 17], and contrasts with studies performed on nanomaterials [42] and/or thin films [10, 11], where due to the finite volume of Pd, the hydrogen adsorption (H_{ads}) and hydrogen absorption (H_{abs}) processes can be distinguished voltammetrically (*i.e.*, where the Pd substrate becomes fully saturated with H_{abs} on the voltammetric timescale).

For comparative purposes, the voltammetric response of Pd was subsequently investigated at the nanoscale in the SECCM format; the CV is shown in Figure 2b. The CV obtained at the nanoscale is superficially similar to that obtained at the macroscale, with processes corresponding to PdO_x

formation, PdO_x stripping and hydrogen adsorption-absorption occurring at potentials above *ca.* 0.6 V, around *ca.* 0.2 V and below *ca.* −0.15 V *vs* Ag/AgCl, respectively. It is interesting to note at the nanoscale, PdO_x formation occurs in a single process (*i.e.*, single peak at *ca.* 0.7 V *vs* Ag/AgCl, Figure 2b), compared to multiple processes at the macroscale (*i.e.*, multiple peaks at *ca.* 0.35, 0.5 and 0.65 V *vs* Ag/AgCl, Figure 2a). This can be understood by considering that the grain size of annealed Pd (10s to 100s μm scale, *vide infra*) is orders-of-magnitude larger than the SECCM probe size (< 1 μm diameter), meaning Figure 2b is effectively a *single crystal measurement* [25], whereas a multitude of grains of different crystallographic orientation are probed simultaneously during the macroscopic measurement in Figure 2a. Considering the hydrogen adsorption-absorption process, as the working electrode area (defined by the meniscus cell) is very small compared to the total volume of the electrode, the Pd foil effectively acts as an 'infinite' sink for H_{abs} in this configuration. Also, as Pd possesses high intrinsic hydrogen solubility and rapid entry kinetics [10, 11, 42], any structural influence on the rate of electrochemical hydrogen absorption will be the result of grain-dependent electron-transfer kinetics for the hydrogen adsorption process (*vide infra*).

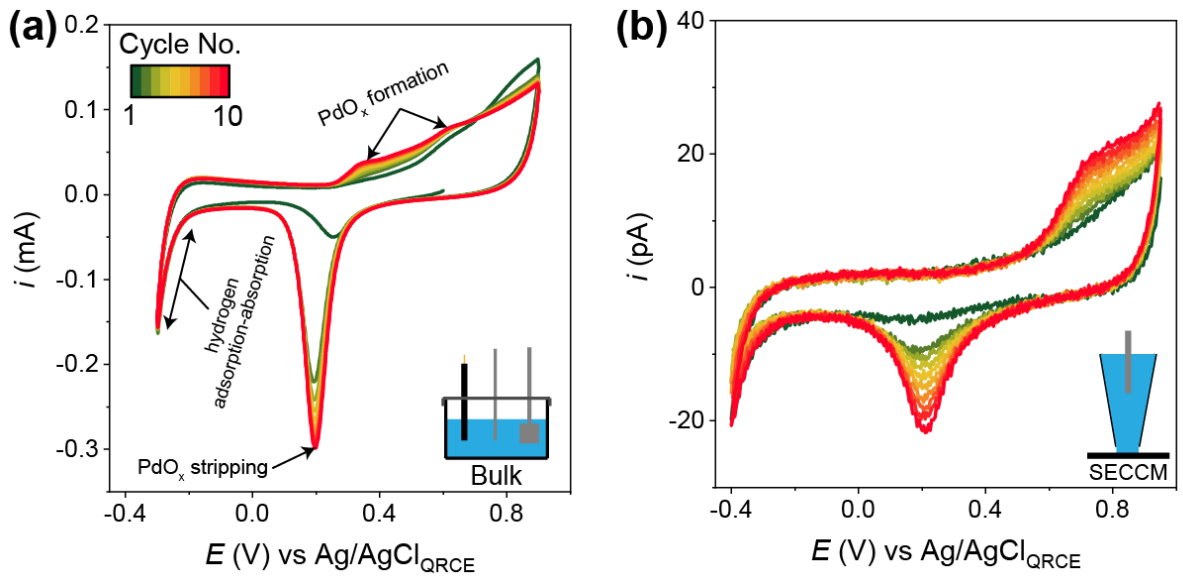

Figure 2. Cyclic voltammograms (CVs) obtained at the **(a)** macroscale, with an annealed Pd wire working electrode in the standard 3-electrode format (electrode area, $A \approx 0.14$ cm^2, voltammetric scan rate, $\upsilon = 0.5$ V s^{-1}) and **(b)** nanoscale, with an annealed Pd foil working electrode in the SECCM format ($A = 6 \times 10^{-9}$ cm^2, $\upsilon = 2$ V s^{-1}). (a) and (b) were carried out in de-aerated 0.5 M H_2SO_4, against a Ag/AgCl reference electrode [QRCE for (b)] for a total of 10 voltammetric cycles.

Grain-dependent electrochemistry of Pd. The grain-dependent electrochemistry of Pd in 0.5 M H_2SO_4 was investigated using the voltammetric hopping-mode of SECCM [43], in which the potential was cycled from 0.95 to − 0.475 V at voltammetric scan rate (υ) 2 V s^{-1} for a total of 5 cycles to create a CV-SECCM movie, as shown in the Supporting Information, Movie S1. The movie depicts the spatially-resolved $i-E$ behavior of a 200 × 175 μm^2 (41 × 35 pixel^2) area of an annealed polycrystalline Pd surface, for which SEM and EBSD images are shown in Figure 3a and b, respectively. The individual meniscus cells wet a circular surface area of *ca.* 800 nm diameter (evident from the individual droplet "footprints" shown in Figure 3a), independent of the underlying grain structure of the surface (Figure 3b). As the individual grains are large (*i.e.*, on the 10s to 100s μm scale, Figure 2b), a relatively large hopping distance of 5 μm was initially used to ensure several grains were interrogated in a single scanning experiment.

Spatially-resolved equipotential images taken from Movie S1 at potentials of 0.7, 0.2, and −0.45 V *vs* Ag/AgCl are shown in Figure 3c, d and e, respectively. Comparison of these spatially-resolved i_{surf} maps with the EBSD map in Figure 3b reveals that PdO_x formation (0.7 V, Figure 3c), PdO_x stripping (0.2 V, Figure 3d) and hydrogen adsorption-absorption (−0.45 V, Figure 3e) are all grain dependent processes. Note that although the current associated with the PdO_x formation/stripping processes increases with cycling (Figure 2b), the relative trends between the individual grains do not, evident from Movie S1. Although not the focus of this study, it is also interesting to note that grains that possess

only subtly different crystallographic orientations (*e.g.*, grains 1 and 11 in Figure 3b) can have very different PdO_x formation/stripping behaviors, as alluded to above. Similar trends are also seen in the case of the hydrogen absorption reaction, explored in greater detail below.

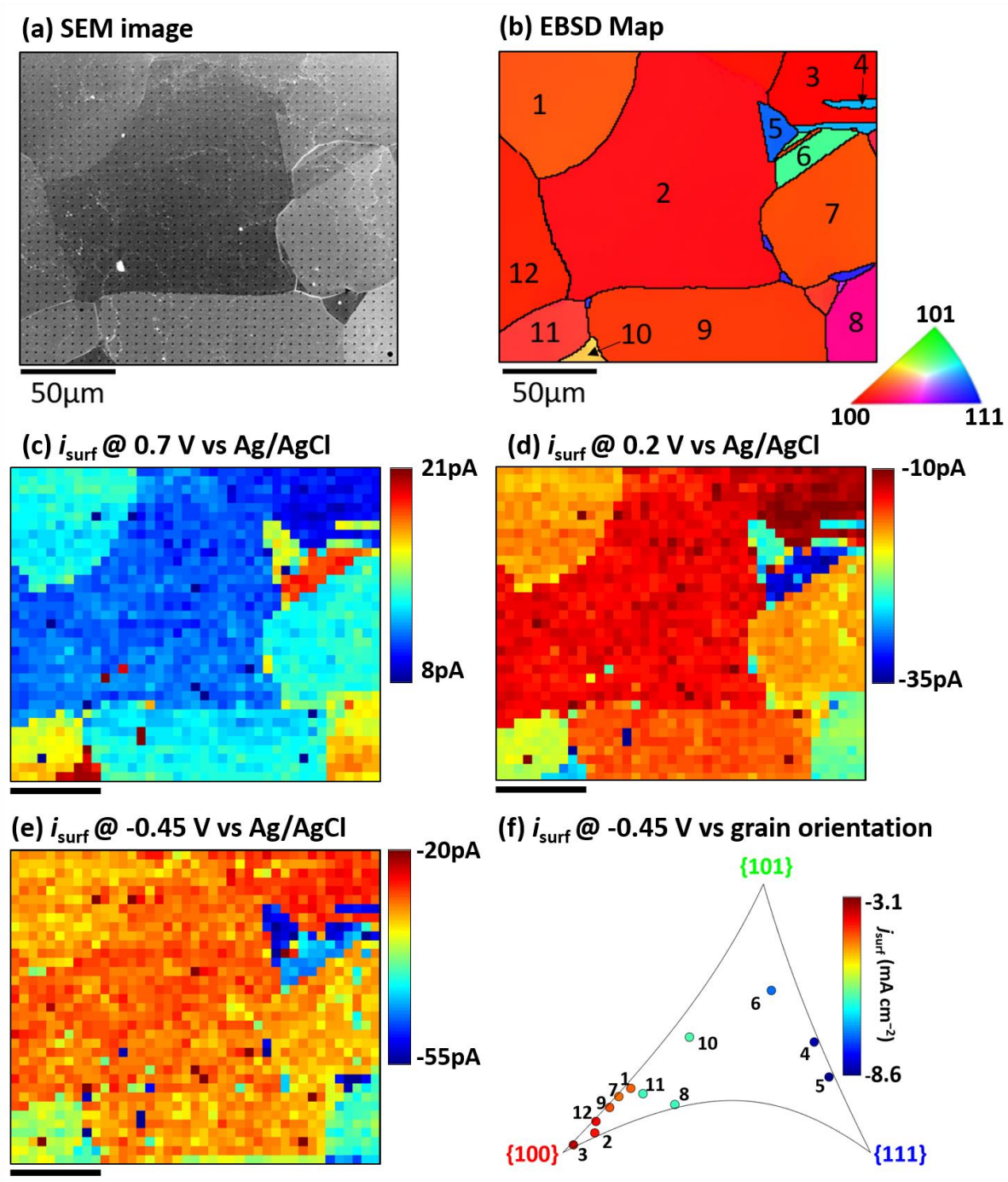

Figure 3. (a) SEM image and **(b)** corresponding EBSD map of an annealed polycrystalline Pd surface, after an SECCM scan. Spatially-resolved equipotential images extracted from the 4th potential cycle of Movie S1, taken

at potentials of **(c)** 0.7 V, **(d)** −0.2 V, and **(e)** − 0.45 V *vs* Ag/AgCl. The scan covers a 200 × 175 μm^2 area comprised of 41 × 35 (1435 total) individual scanning sites (pixels), with a hopping distance of 5 μm. The nanopipet probe contained 0.5 M H_2SO_4 and wetted an area of ≈ 6 × 10^{-9} cm^2 (*i.e.*, i_{surf} of 100 pA ≈ j_{surf} of 15.7 mA·cm^{-2} for the footprint size of 6 × 10^{-9} cm^2). **(f)** Plot of the j_{surf} as a function of the orientation deviation of each grain labelled in (b), relative to the low-index orientations (*i.e.*, {100}, {101} and {111}). The scale bars in (a - e) indicate 50 μm.

Crystallographic dependence of the hydrogen adsorption-absorption reaction. As detailed in the Experimental Section, in order to visualize the grain dependency of the hydrogen adsorption-absorption reaction, a graphical representation of the deviation between the orientations of the grains numbered in Figure 3b and each of the low-index planes (*i.e.*, {100}, {101}, and {111}) was constructed, as shown in Figure 3f. The color of each point represents the average surface current density (j_{surf}) for each grain at − 0.45 V *vs* Ag/AgCl (normalized to the probed area of the meniscus cell to enable comparison with other scans, *vide infra*), which is taken as an indicator of the relative hydrogen absorption kinetics, herein. Evidently, grains with orientations close to the {100} plane (appearing red in color) show the lowest rates of hydrogen absorption. For instance, grain 3, which is the closest to the {100} orientation, at a deviation of 1.8º, is in fact the least active grain within this scan area. Interestingly, while grain 11 is close in orientation to grains 1 and 7, the former facilitates significantly higher hydrogen absorption rates than the latter two, demonstrating that even small changes in orientation can have a major influence on the affinity to hydrogen of a given surface.

Additional scans were carried out on other areas of the annealed polycrystalline Pd surface; examples are shown in Figures 4 and 5. Note that due to differences in the SECCM probe size, the raw i_{surf} values vary significantly from scan-to-scan. Nonetheless, as the area wetted by the meniscus cell (*i.e.*, working electrode area) was measured accurately by SEM imaging (example shown in Figure 3a), comparisons between different scan areas have been made in terms of current density (*i.e.*, j_{surf}). Figure

4a comprises 7 unique grains, each of which possess different electrochemical behavior (*i.e.*, PdO_x formation/stripping and hydrogen absorption), as shown in the Supporting Information, Movie S2. A spatially-resolved equipotential image taken from Movie S2 at a potential of − 0.45 V *vs* Ag/AgCl is shown in Figure 4b, from which data were used to construct the grain-average j_{surf} versus crystallographic orientation plot in Figure 4c. Grain 4, which possesses an orientation close to the {411} high-index plane, is by far the most active (*i.e.*, gave rise to the most negative hydrogen absorption current at − 0.45 V *vs* Ag/AgCl). Incidentally, grain 4 is similar in orientation to grain 8 in Figure 3f, which was also relatively active for hydrogen absorption. Grain 5 is the least active in Figure 4, which has an orientation close to the low-index {101} plane, a deviation of 3.1º. This is consistent with Figure 3f, where the least active grains were also those closest to the low-index orientations (*i.e.*, {100} in Figure 3 and {101} in Figure 4).

Figure 5a comprises 8 unique grains, each of which possess a different electrochemical behavior, as shown in the Supporting Information, Movie S3. A spatially-resolved equipotential image taken from Movie S3 at a potential of − 0.45 V vs Ag/AgCl is shown in Figure 5b, data from which was used to construct the grain-average j_{surf} versus crystallographic orientation plot in Figure 5c. Grains 1 and 7 possess orientations close to the high-index {411} orientation, and exhibit the highest activity, consistent with grain 4 in Figure 5. Conversely, grain 5, which has an orientation close to the low-index {111} plane, a deviation of 4.8º, is the least active. Again, this is consistent with the results from Figures 3 and 4, where the grains with the lowest hydrogen adsorption-absorption activity were those close to the low-index {100} and {101} grains, respectively.

The hydrogen absorption properties of the different crystal facets on Pd is most frequently studied on shape-engineered PdNPs [44]. While it is generally accepted that the shape of PdNPs does

influence the hydrogen uptake rate, the precise relationship between crystallographic structure and function (*i.e.*, absorption kinetics) is not well established [15, 16]. Our results indicate that electrochemical hydrogen absorption is a strongly grain-dependent process, occurring most readily on grains of high-index orientation (*e.g.*, grains close to the {411} plane) compared to those of low-index orientation (*e.g.*, grains close to the {100}, {101} or {111} planes). Limited macroscopic electrochemical studies on Pd single-crystal electrodes also report strongly structure-dependent voltammetric behavior (*i.e.*, PdO_x formation/stripping and/or hydrogen absorption), although such studies only consider the low-index planes [19]. Indeed, two major advantages of the SECCM *pseudo single-crystal approach* [25] are that it avoids the difficult preparation process required for single-crystal electrodes, and additionally allows high-energy surfaces such as high-index grains and grain boundaries (*vide infra*) to be interrogated in a single scanning experiment.

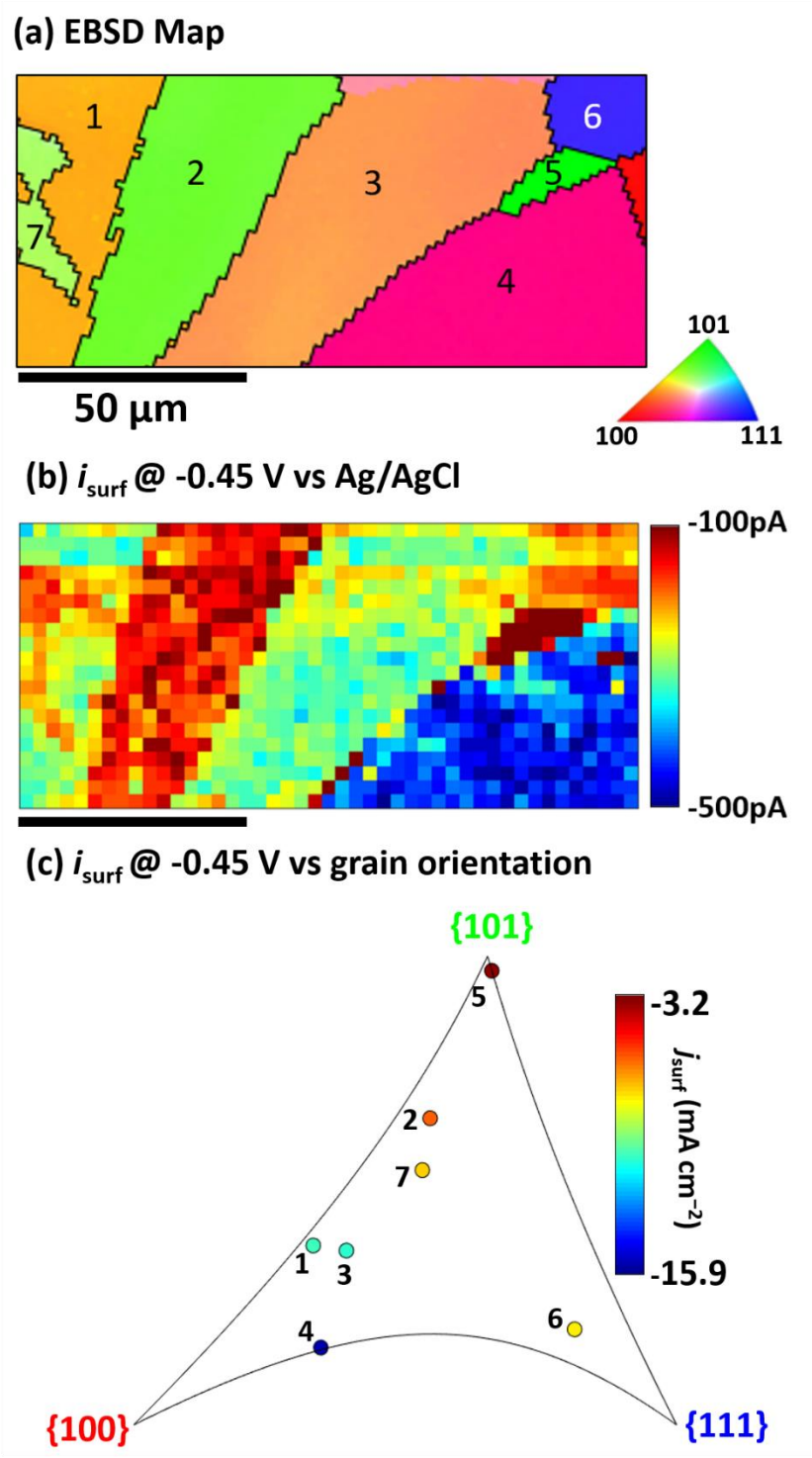

Figure 4. (a) EBSD map of an annealed polycrystalline Pd surface, after an SECCM scan. **(b)** Spatially-resolved equipotential image extracted from the 4th potential cycle of Movie S2, taken at − 0.45 V *vs* Ag/AgCl. The scan covers a 138 × 63 µm area comprising of 45 × 20 (900 total) individual scanning sites (pixels), with a hopping distance of 3 µm. The nanopipet probe contained 0.5 M H_2SO_4 and wetted an area of ≈ 3 × 10^{-8} cm^2 (*i.e.*, i_{surf} of 100 pA ≈ j_{surf} of 3.2 mA·cm^{-2} for the footprint size of 3 × 10^{-9} cm^2). **(c)** Plot of the j_{surf} as a function of the

orientation deviation of each grain labelled in (a), relative to the low-index orientations. The scale bars in (a) and (b) indicate 50 µm.

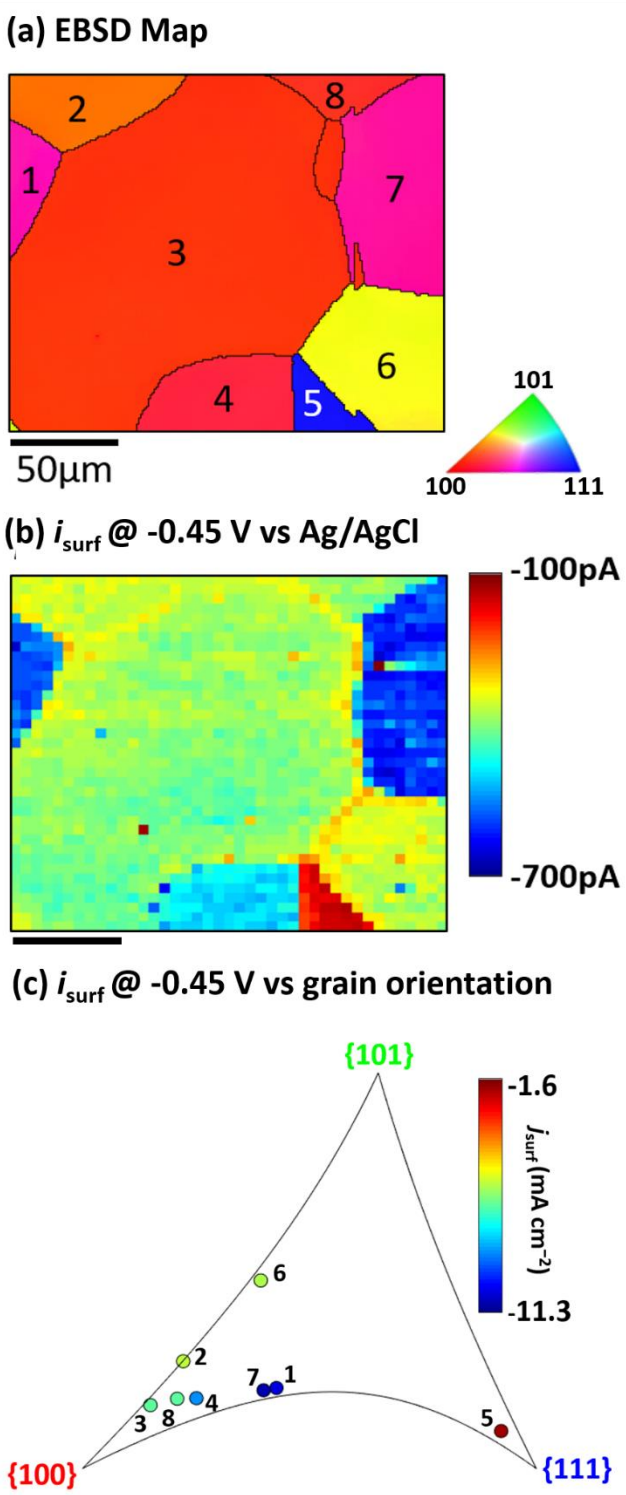

Figure 5. (a) EBSD map of an annealed polycrystalline Pd surface, after an SECCM scan. **(b)** Spatially-resolved equipotential image extracted from the 4th potential cycle of Movie S3, taken at − 0.45 V *vs* Ag/AgCl. The scan covers a 200 × 180 µm area comprising of 41 × 37 (1517 total) individual scanning sites (pixels), with a hopping

distance of 5 μm. The nanopipet probe contained 0.5 M H_2SO_4 and wetted an area of ≈ 6×10^{-8} cm^2 (*i.e.*, i_{surf} of 100 pA ≈ j_{surf} of 1.6 $mA \cdot cm^{-2}$ for the footprint size of 6×10^{-8} cm^2). **(c)** Plot of the j_{surf} as a function of the orientation deviation of each grain labelled in (a), relative to the low-index orientations. The scale bars in (a) and (b) indicate 50 μm.

Hydrogen absorption at grain boundaries. Alluded to above, in addition to presenting a collection of grains of different orientation, polycrystalline metals also possess grain boundaries (*i.e.*, the interface between neighboring crystallites), which have been shown to be electrochemical (electrocatalytic) hotspots for some electrochemical reactions in previous SECCM studies [25, 29, 32]. Comparing the CV-SECCM movies in the Supporting Information, Movies S4 and S5, with the corresponding EBSD maps in Figure 6a-i and 6a-ii, it is clear that specific areas of the annealed polycrystalline Pd possess highly active grain boundaries. Considering the spatially-resolved equipotential images taken from Movies S4 and S5 at a potential of − 0.4 V *vs* Ag/AgCl, shown in Figure 6b-i and 6b-ii, respectively, it is clear that grain boundaries of certain orientations give rise to apparently accelerated hydrogen absorption rates. This observation is consistent with previous reports of accelerated hydrogen diffusion at the grain boundaries of metals such as Pd [45], Ni [46] and Al [47].

Although the data presented in Movie S4, Movie S5 and Figure 6 suggest enhanced hydrogen absorption at grain boundaries with specific geometries, it is important to consider the morphology (topology) of the Pd surface, adjacent to the boundary. Figure 7 presents a detailed examination of a grain boundary where elevated hydrogen absorption currents were detected. A section of the i_{surf} map (originally presented in Figure 6b-i), accompanied by co-located SEM images of the "active sites" is shown in Figure 7a. The SEM images reveal that the flame annealing process has induced a degree of deformation at the grain boundary surface termination. While the formation of a more defective surface could certainly influence electrochemical (electrocatalytic) activity (*vide infra*), surface deformation is

also expected to increase the surface roughness, locally increasing the electrochemically active surface area (ECSA). Indeed, CVs extracted from the active sites (numbered in Figure 7a), presented in Figure 7b, demonstrate that the i_{surf} arising from PdO_x formation/stripping, as well as from double layer capacitance is also larger at the "active" pixels, suggesting an increased ECSA contributes to the elevated hydrogen absorption current at the "active" grain boundaries.

It is also worth noting that atoms with low-lattice coordination numbers present at surface defects such as grain boundaries are postulated to serve as the active sites for (electro)catalytic processes, due to an enhanced ability to bind reactants, and break/form covalent bonds [18, 48, 49]. For instance, it has previously been reported that the rate of hydrogen absorption is higher for shape-controlled PdNPs containing a higher number of vertices, promoted by palladium-hydride phase nucleation at these undercoordinated sites [15]. Due to the surface deformation shown in Figure 7, it is plausible that there is an increased density of surface defects in the regions neighboring the "active" grain boundary. For example, many of the scanning points (pixels) that are shown to be active in Figure 7a (*e.g.*, points 1 and 2), do not lie on the boundary itself, but rather are situated in deformed areas adjacent to the boundary, consistent with a previous SECCM study on electrochemical CO_2 reduction at polycrystalline Au [29]. Thus, while SECCM alone cannot unambiguously distinguish between increased ECSA versus enhanced activity as the source of the local enhancement in i_{surf}, this study highlights that careful analysis of the droplet "footprints" is vital to avoid misleading conclusions about the intrinsic activity of microscopic surface features such as grain boundaries.

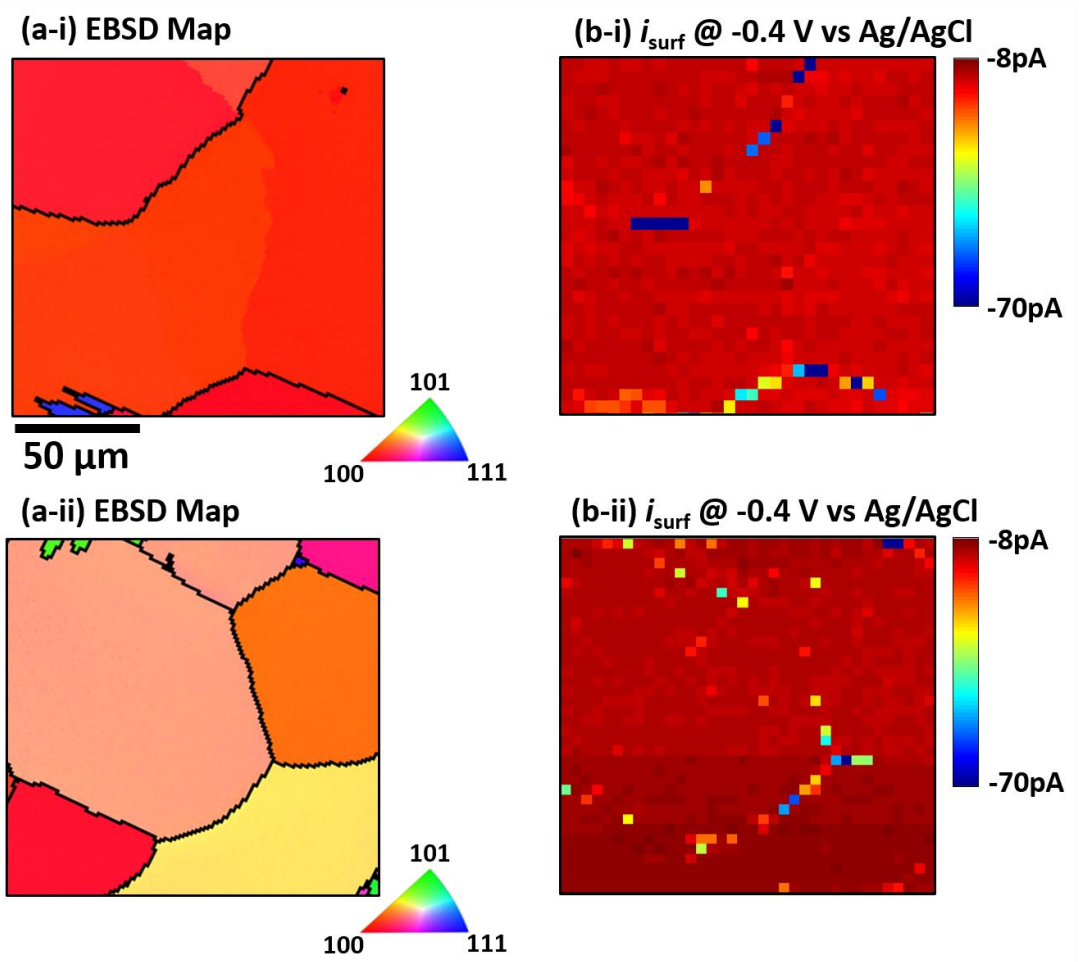

Figure 6. (a) EBSD maps of an annealed polycrystalline Pd surface, after SECCM scans. **(b)** Spatially-resolved equipotential images extracted from the 4th potential cycle of Movies **(i)** S4 and **(ii)** S5, taken at − 0.4 V *vs* Ag/AgCl. The scans consist of **(i)** 30 × 29 sites (870 total) covering 116 × 112 µm, and **(ii)** 36 × 36 sites (1296 total) covering 140 × 140 µm. Both scans employed a hopping distance of 4 µm. The nanopipet probe contained 0.5 M H_2SO_4 and wetted an area of ≈ 1 × 10^{-8} cm^2 (*i.e.*, i_{surf} of 100 pA ≈ j_{surf} of 7.5 mA·cm^{-2} for the footprint size of 1 × 10^{-8} cm^2). All scale bars indicate 50 µm.

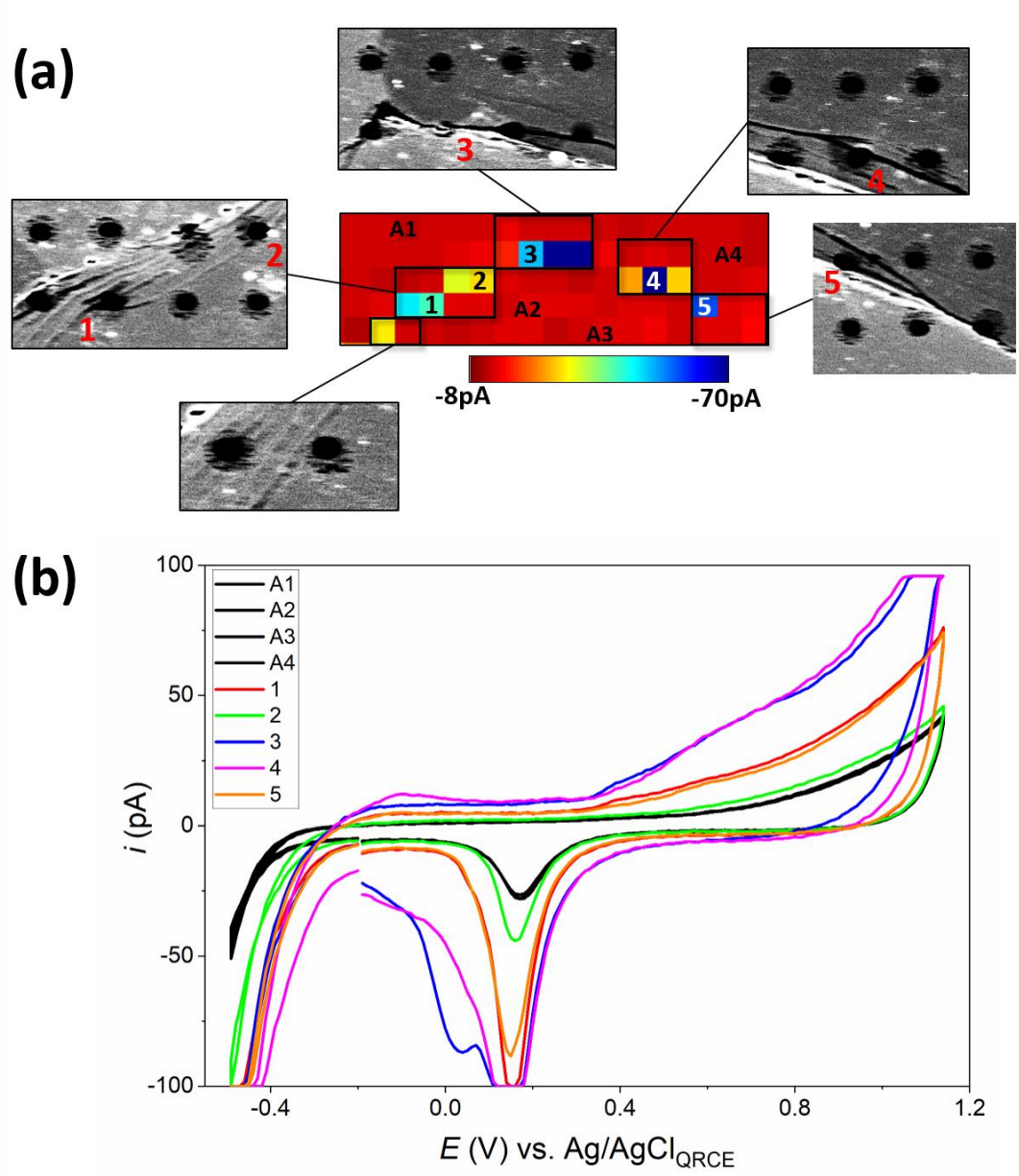

Figure 7. (a) i_{surf} map, recorded with SECCM at − 0.4 V *vs* Ag/AgCl, on an "active" grain boundary of annealed polycrystalline Pd (taken from Figure 6a), accompanied by co-located SEM images of the boxed areas. The distance between pixels (*i.e.*, hopping distance) is 4 µm. **(b)** CVs of the scanning points indicated in (a). The nanopipet probe contained 0.5 M H_2SO_4 and wetted an area of ≈ 1×10^{-8} cm^2 (*i.e.*, i_{surf} of 100 pA ≈ j_{surf} of 7.5 $mA \cdot cm^{-2}$ for the footprint size of 1×10^{-8} cm^2). Note that employed electrometer only measured i_{surf} values within the ±100 pA range.

Conclusions

In this study, using annealed polycrystalline Pd as a model system, it was shown that the rate of electrochemical hydrogen absorption (in 0.5 M H_2SO_4) is strongly influenced by surface structure (*e.g.*, grains and grain boundaries). With the use of SECCM, multi-cycle CVs were collected at different locations on individual grains, which were subsequently identified (*i.e.*, structurally characterized) with EBSD. Through this *correlative electrochemical microscopy approach*, grains close to the low-index orientations (*i.e.* {100}, {101}, and {111} planes of *fcc* Pd) were shown to exhibit the lowest rates of hydrogen absorption, whereas grains with high-index orientations (*e.g.*, {411}) facilitated the highest rates. Enhanced hydrogen absorption currents were measured at some grain boundaries across the surface of polycrystalline Pd, which was attributed to surface deformation giving rise to an increased ECSA and/or high defect density, leading to enhanced hydrogen absorption activity. Overall, these data improve our understanding of how surface structure can influence the ingress of hydrogen into metals, which is particularly important in the areas of corrosion (*e.g.*, hydrogen embrittlement) and energy conversion/storage (*e.g.*, hydrogen generation, purification and storage).

Acknowledgements

This work was supported by an iCASE award to L.Y. from the Engineering and Physical Sciences Research Council (EPSRC, U.K.). C.L.B. acknowledges financial support from the Ramsay Memorial Fellowship Trust (U.K.). P.R.U. gratefully acknowledges support from a Wolfson Research Merit Award (Royal Society, U.K.).

References

[1] B. Pound, in: M. Stratmann, G. Frankel (Eds.) Corrosion and Oxide Films, Wiley-VCH, Germany, 2003, pp. 108-155.

[2] T. Ohtsuka, A. Nishikata, M. Sakairi, K. Fushimi, Electrochemical Fundamentals for Corrosion Fundamentals, Springer 2018.

[3] R.A. Oriani, Hydrogen Embrittlement of Steels, Ann. Rev. Mater. Sci., 8 (1978) 327-357.

[4] J. Woodtli, R. Kieselback, Damage due to hydrogen embrittlement and stress corrosion cracking, Eng. Fail. Anal., 7 (2000) 427-450.

[5] K. Farrell, Cathodic Hydrogen Absorption and Severe Embrittlement in a High Strength Steel, Corrosion, 26 (1970) 105-110.

[6] I.M. Robertson, P. Sofronis, A. Nagao, M.L. Martin, S. Wang, D.W. Gross, K.E. Nygren, Hydrogen Embrittlement Understood, Metall. Mater. Trans. A, 46 (2015) 2323-2341.

[7] O. Barrera, D. Bombac, Y. Chen, T.D. Daff, E. Galindo-Nava, P. Gong, D. Haley, R. Horton, I. Katzarov, J.R. Kermode, C. Liverani, M. Stopher, F. Sweeney, Understanding and mitigating hydrogen embrittlement of steels: a review of experimental, modelling and design progress from atomistic to continuum, J. Mater. Sci., 53 (2018) 6251-6290.

[8] Y. Mine, K. Tachibana, Z. Horita, Grain-boundary diffusion and precipitate trapping of hydrogen in ultrafine-grained austenitic stainless steels processed by high-pressure torsion, Mater. Sci. Eng. A, 528 (2011) 8100-8105.

[9] M.A. Mohtadi-Bonab, J.A. Szpunar, S.S. Razavi-Tousi, Hydrogen induced cracking susceptibility in different layers of a hot rolled X70 pipeline steel, Int. J. Hydrog. Energy, 38 (2013) 13831-13841.

[10] C. Gabrielli, P.P. Grand, A. Lasia, H. Perrot, Investigation of Hydrogen Adsorption-Absorption into Thin Palladium Films. I. Theory., J. Electrochem. Soc., 151 (2004) A1925-A1936.

[11] C. Gabrielli, P.P. Grand, A. Lasia, H. Perrot, Investigation of Hydrogen Adsorption and Absorption in Palladium Thin Films. II. Cyclic Voltammetry, J. Electrochem. Soc., 151 (2004) A1937-A1942.

[12] B.D. Adams, A. Chen, The role of palladium in a hydrogen economy, Mater. Today, 14 (2011) 282-289.

[13] S.K. Konda, A. Chen, Palladium based nanomaterials for enhanced hydrogen spillover and storage, Mater. Today, 19 (2016) 100-108.

[14] G. Li, H. Kobayashi, S. Dekura, R. Ikeda, Y. Kubota, K. Kato, M. Takata, T. Yamamoto, S. Matsumura, H. Kitagawa, Shape-dependent hydrogen-storage properties in Pd nanocrystals: which does hydrogen prefer, octahedron (111) or cube (100)?, J. Am. Chem. Soc., 136 (2014) 10222-10225.

[15] N.J.J. Johnson, B. Lam, B.P. MacLeod, R.S. Sherbo, M. Moreno-Gonzalez, D.K. Fork, C.P. Berlinguette, Facets and vertices regulate hydrogen uptake and release in palladium nanocrystals, Nat. Mater., 18 (2019) 454-458.

[16] S. Dekura, H. Kobayashi, K. Kusada, H. Kitagawa, Hydrogen in Palladium and Storage Properties of Related Nanomaterials: Size, Shape, Alloying, and Metal-Organic Framework Coating Effects, Chemphyschem, 20 (2019) 1158-1176.

[17] M. Grdeń, M. Łukaszewski, G. Jerkiewicz, A. Czerwiński, Electrochemical behaviour of palladium electrode: Oxidation, electrodissolution and ionic adsorption, Electrochim. Acta, 53 (2008) 7583-7598.

[18] C.L. Bentley, M. Kang, P.R. Unwin, Nanoscale Surface Structure-Activity in Electrochemistry and Electrocatalysis, J. Am. Chem. Soc., 141 (2019) 2179-2193.

[19] M. Hara, U. Linke, T. Wandlowski, Preparation and electrochemical characterization of palladium single crystal electrodes in 0.1M $H2SO_4$ and $HClO_4$, Electrochim. Acta, 52 (2007) 5733-5748.

[20] U. Stuhr, T. Striffler, H. Wipf, H. Natter, B. Wettmann, S. Janssen, R. Hempelmann, H. Hahn, An investigation of hydrogen diffusion in nanocrystalline Pd by neutron spectroscopy, J. Alloys Compd., 253-254 (1997) 393-396.

[21] A. Pundt, R. Kirchheim, Hydrogen in Metals: Microstructural Aspects, Annual Review of Materials Research, 36 (2006) 555-608.

[22] N. Ebejer, A.G. Güell, S.C.S. Lai, K. McKelvey, M.E. Snowden, P.R. Unwin, Scanning electrochemical cell microscopy: a versatile technique for nanoscale electrochemistry and functional imaging, Ann. Rev. Anal. Chem., 6 (2013) 329-351.

[23] C.L. Bentley, M. Kang, P.R. Unwin, Scanning electrochemical cell microscopy: New perspectives on electrode processes in action, Curr. Opin. Electrochem., 6 (2017) 23-30.

[24] C.L. Bentley, J. Edmondson, G.N. Meloni, D. Perry, V. Shkirskiy, P.R. Unwin, Nanoscale Electrochemical Mapping, Anal. Chem., 91 (2019) 84-108.

[25] B.D.B. Aaronson, C.H. Chen, H.J. Li, M.T.M. Koper, S.C.S. Lai, P.R. Unwin, Pseudo-Single-Crystal Electrochemistry on Polycrystalline Electrodes: Visualizing Activity at Grains and Grain Boundaries on Platinum for the $Fe^{2+/}Fe^{3+}$ Redox Reaction, J. Am. Chem. Soc., 135 (2013) 3873-3880.

[26] B.D.B. Aaronson, S.C.S. Lai, P.R. Unwin, Spatially Resolved Electrochemistry in Ionic Liquids: Surface Structure Effects on Triiodide Reduction at Platinum Electrodes, Langmuir, 30 (2014) 1915-1919.

[27] C.-H. Chen, K.E. Meadows, A. Cuharuc, S.C.S. Lai, P.R. Unwin, High Resolution Mapping of Oxygen Reduction Reaction Kinetics at Polycrystalline Platinum Electrodes, Phys. Chem. Chem. Phys., 16 (2014) 18545-18552.

[28] Y. Wang, E. Gordon, H. Ren, Mapping the Nucleation of H_2 Bubbles on Polycrystalline Pt via Scanning Electrochemical Cell Microscopy, J. Phys. Chem. Lett., 10 (2019) 3887-3892.

[29] R.G. Mariano, K. McKelvey, H.S. White, M.W. Kanan, Selective increase in CO_2 electroreduction activity at grain-boundary surface terminations, Science, 358 (2017) 1187-1192.

[30] D.-Q. Liu, C.-H. Chen, D. Perry, G. West, S.J. Cobb, J.V. Macpherson, P.R. Unwin, Facet-Resolved Electrochemistry of Polycrystalline Boron-Doped Diamond Electrodes: Microscopic Factors Determining the Solvent Window in Aqueous Potassium Chloride Solutions, ChemElectroChem, 5 (2018) 3028-3035.

[31] L.C. Yule, C.L. Bentley, G. West, B.A. Shollock, P.R. Unwin, Scanning electrochemical cell microscopy: A versatile method for highly localised corrosion related measurements on metal surfaces, Electrochim. Acta, 298 (2019) 80-88.

[32] L.C. Yule, V. Shkirskiy, J. Aarons, G. West, C.L. Bentley, B.A. Shollock, P.R. Unwin, Nanoscale Active Sites for the Hydrogen Evolution Reaction on Low Carbon Steel, J. Phys. Chem. C, 123 (2019) 24146-24155.

[33] L.C. Yule, V. Shkirskiy, J. Aarons, G. West, B.A. Shollock, C.L. Bentley, P.R. Unwin, Nanoscale electrochemical visualization of grain-dependent anodic iron dissolution from low carbon steel, Electrochim. Acta, (2019) 135267.

[34] C.L. Bentley, D. Perry, P.R. Unwin, Stability and Placement of Ag/AgCl Quasi-Reference Counter Electrodes in Confined Electrochemical Cells, Anal. Chem., 90 (2018) 7700-7707.

[35] M.E. Snowden, A.G. Güell, S.C.S. Lai, K. McKelvey, N. Ebejer, M.A. O'Connell, A.W. Colburn, P.R. Unwin, Scanning Electrochemical Cell Microscopy: Theory and Experiment for Quantitative High Resolution Spatially-Resolved Voltammetry and Simultaneous Ion-Conductance Measurements, Anal. Chem., 84 (2012) 2483-2491.

[36] N. Ebejer, A.G. Güell, S.C.S. Lai, K. McKelvey, M.E. Snowden, P.R. Unwin, in: R.G. Cooks, J.E. Pemberton (Eds.) Annual Review of Analytical Chemistry, Vol 6, Annual Reviews, Palo Alto, 2013, pp. 329-351.

[37] C.L. Bentley, P.R. Unwin, Nanoscale Electrochemical Movies and Synchronous Topographical Mapping of Electrocatalytic Materials, Faraday Disc., 210 (2018) 365-379.

[38] C.L. Bentley, M. Kang, P.R. Unwin, Nanoscale Structure Dynamics within Electrocatalytic Materials, J. Am. Chem. Soc., 139 (2017) 16813-16821.

[39] I.M. Ornelas, P.R. Unwin, C.L. Bentley, High-Throughput Correlative Electrochemistry−Microscopy at a Transmission Electron Microscopy (TEM) Grid Electrode, Anal. Chem., 91 (2019) 14854-14859.

[40] M. Kang, D. Perry, C.L. Bentley, G. West, A. Page, P.R. Unwin, Simultaneous Topography and Reaction Flux Mapping at and around Electrocatalytic Nanoparticles, ACS Nano, 11 (2017) 9525-9535.

[41] S. Trasatti, Work Function, Electronegativity, and Electrochemical Behvaiour of Metals. III. Electrolytic Hydrogen Evolution in Acid Solutions, J. Electroanal. Chem., 39 (1972) 163-184.

[42] A. Zalineeva, S. Baranton, C. Coutanceau, G. Jerkiewicz, Electrochemical behavior of unsupported shaped palladium nanoparticles, Langmuir, 31 (2015) 1605-1609.

[43] C.-H. Chen, L. Jacobse, K. McKelvey, S.C.S. Lai, M.T.M. Koper, P.R. Unwin, Voltammetric Scanning Electrochemical Cell Microscopy: Dynamic Imaging of Hydrazine Electro-oxidation on Platinum Electrodes, Anal. Chem., 87 (2015) 5782-5789.

[44] Y. Xia, Y. Xiong, B. Lim, S.E. Skrabalak, Shape-controlled synthesis of metal nanocrystals: simple chemistry meets complex physics?, Angew. Chem.-Int. Ed. Engl., 48 (2009) 60-103.

[45] H. Iwaoka, M. Arita, Z. Horita, Hydrogen diffusion in ultrafine-grained palladium: Roles of dislocations and grain boundaries, Acta Mater., 107 (2016) 168-177.

[46] A.M. Brass, A. Chanfreau, Accelerated Diffusion of Hydrogen along Grain Boundaries in Nickel, Acta Mater., 44 (1995) 3823-3831.

[47] M. Ichimura, Y. Sasajima, M. Imabayashi, Grain Boundary Effect on Diffusion of Hydrogen in Pure Aluminum, Mater. Trans., 32 (1991) 1109-1114.

[48] M.T. Koper, Structure sensitivity and nanoscale effects in electrocatalysis, Nanoscale, 3 (2011) 2054-2073.

[49] A.P. O'Mullane, From single crystal surfaces to single atoms: investigating active sites in electrocatalysis, Nanoscale, 6 (2014) 4012-4026.